Received: 14 March 2023 | Accepted: 7 January 2024

DOI: 10.1002/jpln.202300080

RESEARCH ARTICLE

Coupling scales in process-based soil organic carbon modeling including dynamic aggregation

Simon Zech[1] | **Alexander Prechtel**[1] | **Nadja Ray**[2]

[1]Department of Mathematics, Applied Mathematics (Modelling and Numerics), Friedrich-Alexander-Universität Erlangen-Nürnberg (FAU), Erlangen, Germany

[2]Mathematical Institute for Machine Learning and Data Science, Katholische Universität Eichstätt-Ingolstadt, Ingolstadt, Germany

Correspondence
Alexander Prechtel, Department of Mathematics, Applied Mathematics (Modelling and Numerics), Friedrich-Alexander-Universität Erlangen-Nürnberg (FAU), Erlangen, Germany.
Email: prechtel@math.fau.de

This article has been edited by Kai Uwe Totsche.

Funding information
Deutsche Forschungsgemeinschaft, Grant/Award Number: 276972051

Abstract

Background: Carbon storage and turnover in soils depend on the interplay of soil architecture, microbial activities, and soil organic matter (SOM) dynamics. For a fundamental understanding of the mechanisms that drive these processes, not only the exploitation of advanced experimental techniques down to the nanoscale is necessary but also spatially explicit and dynamic image-based modeling at the pore scale.

Aim: We present a modeling approach that is capable of transferring microscale information into macroscale simulations at the profile scale. This enables the prediction of future developments of carbon fluxes and the impact of changes in the environmental conditions linking scales.

Method: We consider a mathematical model for CO_2 transport across soil profiles (macroscale), which is informed by a pore-scale (microscale) model for C turnover. It allows for the dynamic, self-organized re-arrangement of solid building units, aggregates and particulate organic matter (POM) based on surface interactions, realized by a cellular automaton method, and explicitly takes spatial effects on POM turnover such as occlusion into account. We further include the macroscopic environmental conditions water saturation, POM content, and oxygen concentration.

Results: The coupled simulations of macroscopic transport and pore-scale carbon and aggregate turnover reveal the complex, nonlinear interplay of the underlying processes. Limitations by diffusive transport, oxygen availability, texture-dependent occlusion and turnover of OM drive CO_2 production and carbon storage.

Conclusions: This emphasizes the need for such micro–macro models exchanging information on different scales to investigate and quantify the effects of structural changes, variations in environmental conditions, or degradation processes on carbon turnover.

KEYWORDS

carbon turnover, cellular automaton method, diffusion equation mechanistic image-based modeling, pore-scale model, soil structure dynamics, upscaling

1 | INTRODUCTION

The interplay of soil architecture, microbial dynamics, and SOM turnover determines key functions of soils, such as their capability to store organic carbon (OC; Stockmann et al., 2013). The prediction of the fate of carbon in soils or the impact of changes in the environmental conditions requires a fundamental understanding of the underlying processes at different scales. This necessitates the implementation of novel modeling approaches and, together with advanced experimental techniques down to the nanoscale, allows to challenge coherent hypotheses (Baveye et al., 2018; Gerke et al., 2022; Roose et al., 2016; Totsche et al., 2018; Vereecken et al., 2016). Several recent reviews point out the importance of incorporating process mechanisms at the pore scale in models to better understand carbon turnover in soils (Baveye et al., 2018; Meurer et al., 2020; Pot et al., 2022a, 2022b; Vereecken et al., 2016). On the other hand, environmental ambient conditions such as soil texture, water saturation, carbon content, or oxygen content are highly variable in space and time. Experiments and also simulations show that these macroscopic conditions affect the microbial turnover of SOM and carbon storage and turnover severely (Baveye et al., 2018; Keiluweit et al., 2016; Kuzyakov & Blagodatskaya, 2015; Nunan, 2017; Pot et al., 2022b; Witzgall et al., 2021).

However, macroscale models can consider microscale heterogeneities and structural influences only via averaged parameters. Since the underlying processes are complex, this leads to nonlocal (in space and time) interrelations, which are poorly represented by constant parameters. In contrast to merely heuristic or lumped parameter models, a modeling approach with predictive capability requires that soil structure dynamics is taken into account in a temporally and spatially explicit way (Gerke et al., 2022; Pot et al., 2022b; Stockmann et al., 2013). Only then the influence of, for example, the physical protection of organic matter (OM) on its turnover can be evaluated in detail. This stabilization of OM is a microscale process directly related to aggregation. It is due to its physical separation from decomposers, enzymes, or the necessary components of aerobic decomposition, namely, oxygen and water on the pore scale (Christensen, 2001; McCarthy et al., 2008; Schmidt et al., 2011).

While spatially and temporally explicit models can be used on the microscale to assess the interplay of different processes and properties, the application of these models on a scale of meters or kilometers is not computationally feasible (Roose et al., 2016; Vereecken et al., 2016). In the last decade, some authors have addressed the challenge of upscaling information from the explicit pore scale to the lab/field scale for carbon turnover models. Ebrahimi and Or (2016, 2018) used idealized spherical aggregates and pore network models to incorporate structural microscale information. They noted that aggregate and pore size distributions substantially influence substrate and oxygen diffusion rates and thus regulate the dynamics of microbial communities and subsequently the greenhouse gas fluxes in soils. Chakrawal et al. (2020) compared spatially heterogeneous SOM and biomass distributions at the pore scale to spatially homogeneous conditions and studied the influence, for example, on the mean respiration rate at the soil core scale. They concluded that models assuming homogeneous pools cannot appropriately describe microscale heterogeneities, in particular the collocation of microorganisms and substrates, which strongly affect carbon fluxes in soils. Mbé et al. (2022) simulated microscale scenarios and derived an accessibility coefficient based on the geodesic distance between microorganisms and OM weighted by the amount of OM to explain macroscopic CO_2 fluxes.

All the previous works used either parameter functions to summarize structural properties of the soil or worked on explicit but fixed pore scale geometries. Crawford et al. (1997) presented the first concepts of Monte-Carlo simulations dealing with an explicit evolution of soil structures under the influence of bonding laws and extended this further to explain the self-organization of soil structures under microbial activity changes (Crawford et al., 2012). Applying these ideas within a cellular automaton model (CAM), Tang and Valocchi (2013) investigated biofilm development. Zech, Ritschel, et al. (2022) further adapted and applied the CAM model to study microbial population dynamics and the turnover of POM in microaggregates based on static micro-computed tomography (μCT) images. Using the framework of a CAM, Ray et al. (2017) introduced a process-based mathematical model for the dynamic, self-organized re-arrangement of solid building units, aggregates and POM based on surface interactions.

Zech et al. (2020) and Zech, Schweizer, et al. (2022) extended the dynamic re-arrangement of soil structure to experimental data of the shape of microaggregates (<250 μm) and primary particles gained from dynamic image analyses of wet-sieved fractions of two agricultural topsoils with different clay contents (Schweizer et al., 2019).

In summary, the following challenges outlined above are addressed in this research:

- Modeling carbon turnover on the pore scale (μm), capturing structural dynamics, and depth-dependent environmental conditions with a spatially and temporally explicit microscale model.
- Modeling CO_2 transport on the macroscale, that is, profile scale (dm–m), under the impact of depth-dependent environmental conditions.
- Integrating the information gained on the microscale in the macroscale model.

More precisely, the concept of process-based structure evolution in space and time is integrated into a coupled two-scale approach, that is, solving a series of microscale problems in a layered soil profile and coupling them with a macroscale model describing the diffusive transport of CO_2. Exemplarily, we apply the concept to a virtual soil profile of 0.5-m depth with key environmental factors, namely, water saturation, oxygen, and organic carbon (OC) content, which affect the microscale aggregate and carbon turnover. On the other hand, the CO_2 produced by the microbial degradation of POM at the pore scale acts as a source in the macroscale problem of CO_2 diffusion in the soil. Finally, the effective diffusion coefficient on the macroscale depends on the given saturation of the respective soil layer.

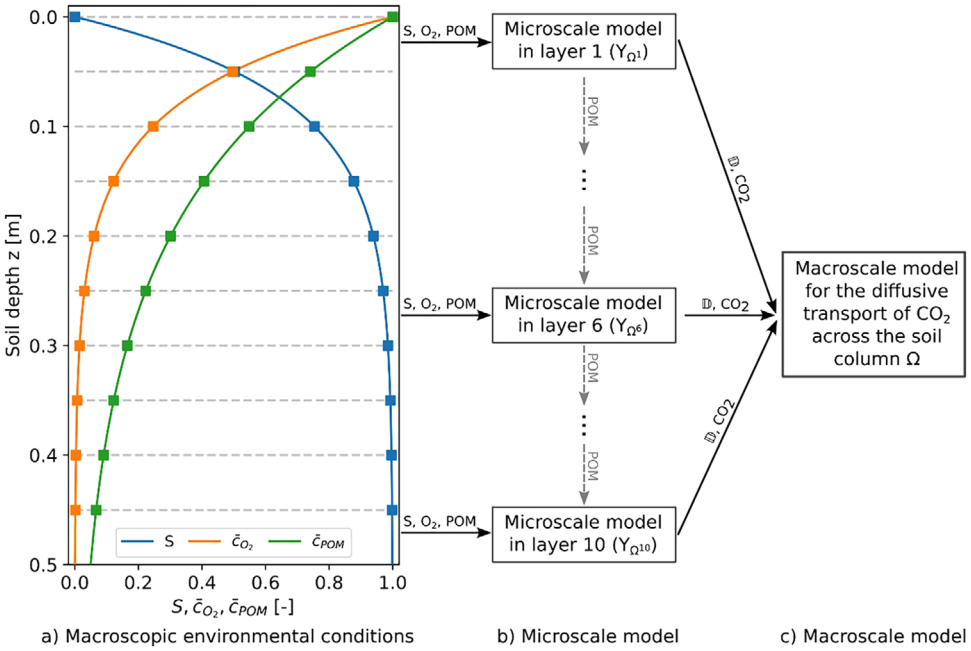

FIGURE 1 Schematic overview of the components of the macroscale model: Environmental conditions for water saturation S, oxygen concentration c_{O2}, and POM concentration c_{POM} (a), microscale model for each layer on the representative domain Y_{Ω_i} parameterized by macroscopic environmental conditions (b), and macroscale model parameterized by the output of microscale model (c).

This approach allows us to study if and how small-scale processes affect carbon storage and turnover and greenhouse gas emissions, and how relevant information can be transferred to a macroscale model. We vary in silico the soil texture and the transfer of unbound POM to deeper layers. While keeping the depth-dependent environmental conditions fixed with respect to time, we study in contrast the impact of spatially variable saturation, oxygen availability, and carbon contents on the overall CO_2 respiration. In addition, limitations in its diffusive transport to the soil surface and accumulation of the produced CO_2 in the soil can be accounted for. The grand goal of the study is the development of a modeling framework that allows to study the interplay of the aforementioned processes and variations under precisely defined conditions in forward simulations, which are based on realistic parameters and insights from experimental studies.

2 | MATERIAL AND METHODS

2.1 | Model concept

We consider a coupled two-scale model, which includes a simple mathematical model for purely diffusive CO_2 transport across the soil profile (macroscale), which is informed by a pore-scale (microscale) model for C turnover. As illustrated in Figure 1, the macroscopic soil profile is divided into a fixed number of layers of equal height. For each layer, we determine the amount of respired CO_2 from a representative microscale model. On these microscale domains, we apply an extension of the spatially and temporally explicit model introduced in Zech, Schweizer, et al. (2022) to calculate the amount of respired CO_2 based on soil texture, water saturation, oxygen concentration, and POM content. These ambient environmental conditions vary vertically along the soil profile (Figure 1). The microscale problems are moreover coupled to one another since unbound POM can potentially be passed to the microscale problem representing the subsequent layer. Finally, based on these inputs, the macroscale spreading of CO_2 in the soil profile is considered (Figure 1).

In the following Section 2.2, we introduce the detailed macroscale model equations. In Section 2.3, we give an overview of the microscale model based on Zech, Schweizer, et al. (2022). In Section 2.4, we specify the ambient environmental conditions and parametrizations of macro- and microscale models and define different simulation scenarios. The latter allows quantifying the differences in CO_2 production resulting from three soil textures and three options of additional POM input from the overlying soil layer.

2.2 | Macroscale model

We describe the diffusive transport of microbially produced CO_2 with concentration c_{CO_2} across a soil column. We consider a one-dimensional soil column $\Omega = [0, 0.5]$ m aligned along the z-axis consisting of $i = 1, \ldots, 10$ layers Ω_i of the same size defined by $\Omega_i := [(i-1) \times 0.05,\ i \times 0.05]$m for $i \in \{1, \ldots, 10\}$. The macroscopic transport equation in the layered domain Ω is given by

$$\partial_t c_{CO_2}(z,t) - \nabla \cdot \left(D_i \nabla c_{CO_2}(z,t)\right) = f_i^{micro} \text{ in } (0,T) \times \dot{}_i,\ i = 1, \cdots, 10. \quad (1)$$

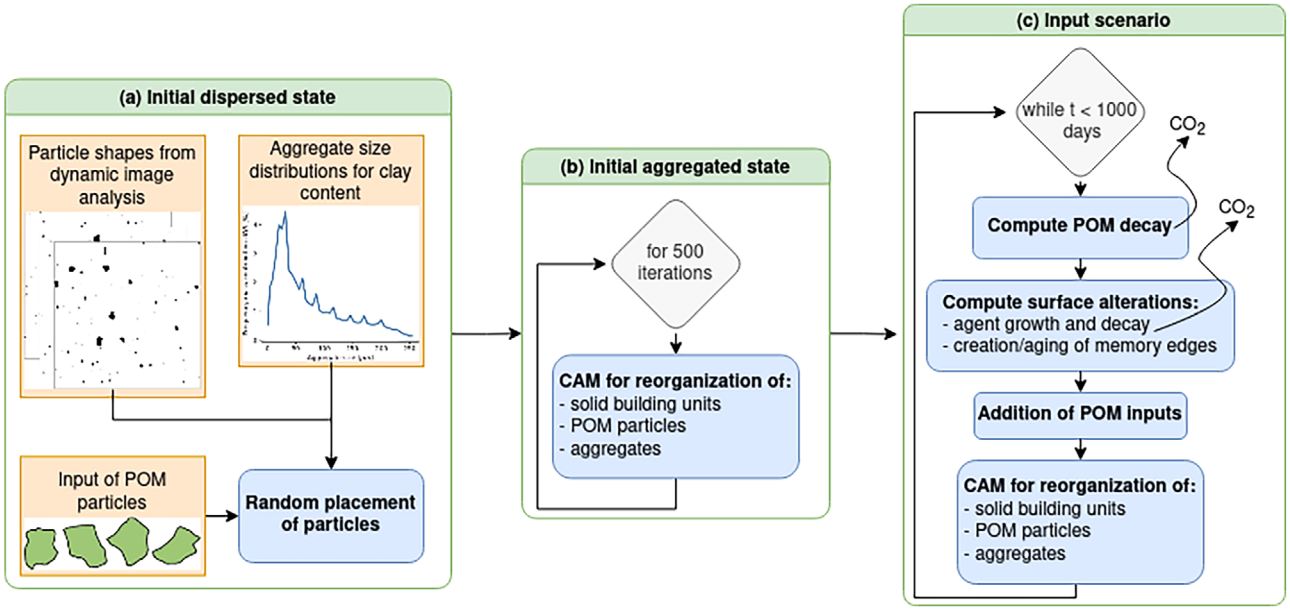

FIGURE 2 Overall workflow of the microscale model: Creation of initial dispersed state (a), application of cellular automaton model (CAM) for creation of aggregated initial state (b), and different input scenarios (c). We also indicate the processes where OM is mineralized to CO_2.

We ensure that the system is at equilibrium initially by choosing the initial CO_2 concentration to be zero and applying a zero Dirichlet boundary condition at the top of the domain. On the bottom of the domain, we consider no-flow boundary conditions:

$$c_{CO_2}(0,t) = 0 \text{ for } t \in (0,T), \tag{2a}$$

$$\nabla c_{CO_2}(0.5,t) \cdot n = 0 \text{ for } t \in (0,T), \tag{2b}$$

$$c_{CO_2}(z,0) = 0 \text{ in } \cdot. \tag{2c}$$

Based on the amount of respired CO_2 in the microscale simulation, we prescribe the source term f_i^{micro} in each layer, see below in Section 2.3.3.

The effective gas diffusion coefficient D_i in the macroscale equations depends on the saturation, which varies from layer to layer and can be determined by different approaches, for example, mathematical upscaling techniques (Ray et al., 2018) or semi-empirical models such as the widely used model by Millington and Quirk (1961), which is based on theoretical calculations for a system of pores and will be used in this study to describe the space dependency (while being constant with respect to time; see Section 2.4).

2.3 | Microscale model

We extend and apply the mechanistic, spatially, and temporally explicit microscale model that has been introduced in Zech, Schweizer, et al. (2022). It describes the interaction between the dynamic rearrangement of inseparable solid building units, the turnover of POM, and simultaneous soil surface alterations in a 2D setting. The workflow for the microscale models is depicted in Figure 2. Below, we give a short overview of the microscale model components and refer to Zech, Schweizer, et al. (2022) for an extended description. In addition, we here include oxygen as a reactant required for the decomposition of POM. We further extend the model by a mechanism that allows passing through unbound, that is, not attached POM to lower layers in the soil column.

2.3.1 | Microscale domain and generation of initial disperse state

As outlined in Section 2.1, we associate a representative microscale domain Y_{Ω_i} to each layer Ω_i. More precisely, we consider two-dimensional domains Y_{Ω_i} of size 500 × 500 µm (250 × 250 pixels with a resolution of 2 µm) where we distinguish explicitly between solid phase, POM particles, and pore space (Figure 3). The solid phase consists of inseparable solid building units, whose shapes are obtained from dynamic image analysis of wet-sieved, water-stable primary soil particles and aggregates of a Cambiosol (see Figure 2a in the workflow and Figure 3 for a sketch; Felde et al., 2021; Schweizer et al., 2019). This arable Cambiosol shows a range of clay contents (Schweizer et al., 2019), and we use the collection of particle shapes and particle size distributions to generate virtual soils with textures of 18% and 33% clay-sized particles (<6.3 µm). The initial dispersed state is created as follows: Solid building units are distributed randomly within the computational domains Y_{Ω_i} according to a prescribed particle size distribution and for a prescribed clay content of either 18% clay (low clay soil) or 33% (high clay soil) and solid phase fraction of 65% (Figure 2a). We choose the same solid phase fraction for both textures to gain com-

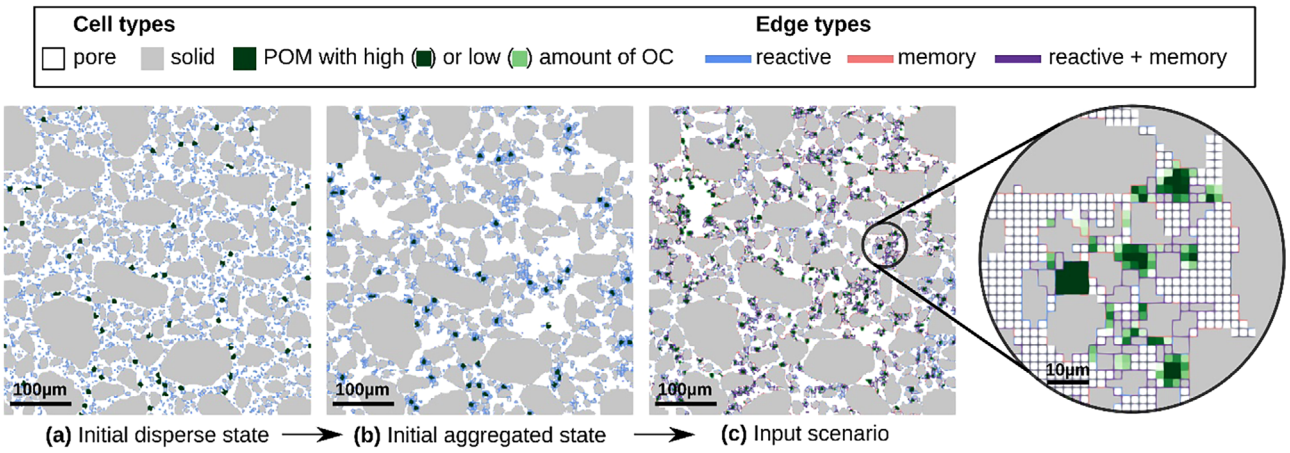

FIGURE 3 Exemplary state of the computational domain for a clay content of 18% after different steps of the microscale model (cf. Figure 2) from the initial dispersed state (a) to initial aggregated state (b) and state after input scenario (c) with schematic representation showing pixels of type solid (gray), pore (white), or POM with different amounts of organic carbon (OC): high (dark green) or low (light green) and edges of type reactive (blue), nonreactive (black), memory (pink), or both reactive and memory (purple).

parable quantities related to the solid phase. Figure 3a shows such an exemplary, initial dispersed state for the soil with 18% clay content. Parts of the surface of the solid building units are marked as reactive, where the share of the reactive surface increases with decreasing particle size. According to the logarithmic decrease of the specific surface area (SSA) with mineral particle sizes (Borkovec et al., 1993) and the increasing relative proportion of clay minerals (Fernández-Ugalde et al., 2013, 2016; Schjønning et al., 1999), we assign 10% of the surface as reactive for sand-sized particles (>63 µm), 25% for coarse silt-sized (>20 µm, <63 µm), 50% for medium silt-sized (>6.3 µm, <20 µm), and 100% of the surface for fine silt and clay-sized particles (<6.3 µm). These reactive edges facilitate aggregation between solid building units and allocation of POM. Finally, POM particles with minimum Feret diameters of 6–10 µm are added to the microscopic computational domains Y_{Ω_i}, while the amount depends on the depth of the respective soil profile layer as outlined in Section 2.4.1 below. On this initial dispersed state (Figures 2a and 3a), we apply our CAM with the rules outlined below to obtain an initial aggregated state resembling a snapshot of a real soil where POM particles are attached to and occluded within the solid matrix (Figure 2b for the workflow and Figure 3b for an example situation). Generating this initial aggregated state leads to a decrease in SSA for all microscale problems, that is, in every layer and for both textures. In the top layer, SSA, for instance, drops from 0.178 to 0.138 μm^{-1} for the 18% clay soil and from 0.233 to 0.168 μm^{-1} for the 33% clay texture. This initial aggregated state represents the starting point ($t = 0$) for the different scenarios in the 1000 days simulations (Figures 2c and 3c).

2.3.2 | CAM for reorganization

Within the pore space, solid building units and POM particles can relocate due to attractive forces. Besides the creation of the initial aggregated state, the CAM rules are applied in combination with the decomposition of POM and surface alterations in every time step, each corresponding to a timespan of 1 day (Figure 2c). The time steps in the CAM are chosen in such a way that they correspond to diffusive ranges, which are realistic for the considered particle sizes, see also Table 1.

Aggregates of solid building units and POM particles, separate solid building units, and POM particles relocate to achieve the most attractive and stable configuration. The range of potential movement decreases with increasing size of the solid building unit, aggregate or POM particle. Following the Stokes–Einstein relation for the diffusion of spherical particles in a liquid and the reasoning of Rupp et al. (2019), this represents the range of Brownian motion, where the mean displacement is equivalent to the expected mean path length and is proportional to the effective radius $1/\sqrt{area}$, with the area of the particle. This resulted in ranges between 10 µm, for entities smaller than 100 μm^2, to 2 µm for entities with an area between 1600 and 80,000 μm^2. For larger aggregates, the range is set to 0. The attractivity is determined based on the amount and type of contact with surfaces with adhesive properties that alter over time due to POM degradation as described in Section 2.3.3. In addition, we include a mechanism allowing for a random break-up of structures where the probability of random break-up and thus underlying stability depended on the types of surface contacts as well. Due to the addition and decomposition of POM particles and related temporal development of surface types (see Section 2.3.3) the most attractive configuration changes with time and is essential to consider since it influences in return the POM turnover. Note that these rules and the explicit spatial representation of the particles allow us to distinguish stable from unstable bindings and occluded from easily accessible POM.

2.3.3 | POM decomposition and surface alteration

Starting from the aggregated initial state (Figure 3b), we apply a combination of the CAM for the structural reorganization with a model

TABLE 1 Variables and parameters in micro- and macroscale model.

Symbol	Parameter	Specification	Unit	Value
Microscale model				
c^p_{POM}	Amount of organic carbon in POM particle p		(g C cm^{-3})	–
k_{POM}	POM decomposition rate		(d^{-1})	0.0239
k_{agent}	POM agent decomposition rate		(d^{-1})	0.0359
–	Minimum agent concentration		(g C cm^{-3})	0.0048
–	Maximum agent concentration		(g C cm^{-3})	0.48
CUE	Carbon use efficiency		(–)	0.45
c_{O_2}	Oxygen concentration		(mg L^{-1})	–
Kc_{O_2}	Half saturation constant oxygen		(mg L^{-1})	10^−3
–	Range of movement	Particle/aggregate size		
–		<100 μm^2	(μm)	10
–		$\in$ [100 μm^2, 176 μm^2]	(μm)	8
–		$\in$]176 μm^2, 400 μm^2 [	(μm)	6
–		$\in$ [400 μm^2, 1600 μm^2 [	(μm)	4
–		$\in$ [1600 μm^2, 80,000 μm^2]	(μm)	2
–		>80,000 μm^2	(μm)	0
–	Attractivity of edge contact	Contact type		
–		Solid (reactive/memory) - solid (reactive/memory)	(–)	1
–		POM–solid (reactive)	(–)	5
–		POM–solid (memory)	(–)	10
–	Probability of random break-up	Contact type		
–		Solid (reactive/memory) - solid (reactive/memory)	(–)	0.25
–		POM–solid (reactive)	(–)	0.1
–		POM–solid (memory)	(–)	0.05
Environmental conditions				
–	Max. initial POM amount		(mg C g^{-1})	3.60
–	Max. POM input rate		(mg C g^{-1} y^{-1})	11.9
	Maximum oxygen concentration		(mg L^{-1})	0.1
Macroscale model				
c_{CO_2}	Macroscopic CO_2 concentration		(mg L^{-1})	–
D^0_g	Molecular diffusion of CO_2 in air		(cm^2 s^{-1})	0.16
D^0_w	Molecular diffusion of CO_2 in water		(cm^2 s^{-1})	1.67-E5
D_i	Effective gas diffusion coefficient in layer i		(cm^2 s^{-1})	–
f^{micro}_i	Source term in layer i		(mg L^{-1} d^{-1})	–

describing the decomposition of POM and simultaneous spreading of microbially produced agents on the solid surface. Zech, Schweizer, et al. (2022) assume that POM particles are degraded with a first-order rate, similar as in Portell et al. (2018), by an immobile microbial population on the reactive solid edges, which itself is not modeled explicitly. The degradation would lead to dissolved OC (DOC) as an intermediate product, which is consumed comparably fast. Zech, Ritschel, et al. (2022) demonstrated that on the pore scale, the diffusion of DOC is sufficiently fast, and only the connectivity of the liquid phase could limit degradation locally. Overall degradation kinetics were identical. Consequently, we do not model this step separately but rather subsume it in the overall degradation rate. We additionally include oxygen as an important reactant required for the decomposition of POM (Keiluweit et al., 2016; Witzgall et al., 2021) and thus considered Monod kinetics (Borden & Bedient, 1986; Ebrahimi & Or, 2016) with respect to oxygen concentration c_{O_2} and linear kinetics with respect to POM concentration c^p_{POM} in the reaction rate:

$$\partial_t\, c^p_{POM} = -k_{POM}\alpha^p_{occ}\,\frac{c_{O_2}}{K_{O_2}+c_{O_2}}\,c^p_{POM}. \tag{3}$$

Here, k_{POM} denotes the POM decomposition rate, $\alpha^p_{occ} \in [0, 1]$ an "occlusion" factor determined by the number of surface contacts of a POM particle p (cf. Zech, Schweizer, et al., 2022, for more details), c^p_{POM} the amount of OC in a POM particle p, c_{O_2} the oxygen concentration in the respective layer, and K_{O_2} the half saturation constant for oxygen. The occlusion factor allows us to take into account that the POM decomposition decreases when it has less contact with pore space and thus is less accessible for microbes. When a POM particle is degraded, part of its OC is taken up by a simultaneously created microbially produced agent on the solid surface in a proportion depending on the carbon use efficiency $CUE = 0.45$, according to the CENTURY model for below-ground OM decomposition (Manzoni et al., 2012). The remainder is released as CO_2-C. From the amount of produced CO_2-C in the microscale domain representative for each layer i, we then calculate the CO_2 production rate, which corresponds to the source term f_i^{micro}.

The microbially produced agent spreads on the solid surface if it exceeds a prescribed threshold and, in this manner, increases its surface coverage. At solid edges where the agent concentration exceeds a minimum threshold, a gluing spot, which enhances the formation of aggregates, is created (Bucka et al., 2019). The agent itself is also degraded, this process again releases CO_2, which contributes to the source term f_i^{micro}. The gluing property may be locally retained even after degradation of the agent coating, and we introduce the term "memory edges" to account for the lasting increase of the mineral surface reactivity of such surface conditioning.

These memory edges are considered the most attractive and stable for the aggregate formation realized by the CAM. Additionally, memory edges have the same function for degradation of POM as reactive edges, that is, POM particles underwent degradation in contact with memory edges in the same manner as described above. Due to an assumed aging process, which may lead to the loss of attractive surface properties, memory edges could also lose their attractive properties over time.

At specified time steps, a certain amount of new POM input is given into the system by placing a layer-dependent number of POM particles of size 15 pixels, corresponding to 60 μm^2, randomly into the pore space of the respective representative microscale domain according to the carbon content decreasing with depth in the soil profile (see the macroscopic boundary conditions in Section 2.4.1). Additionally, we optionally removed all POM particles that were unbound, that is, without contact to a reactive/memory edge for a given number of consecutive days (depending on the scenario, see Section 2.4.4), from the microscale domain. At the same time step, they were then placed randomly within the pore space of the microscale domain being representative to the layer below (Figure 1).

2.4 | Model parametrization and scenarios

2.4.1 | Macroscopic environmental conditions

The water saturation and the derived effective diffusion coefficient, the carbon content in terms of POM, and the oxygen concentration are varied over the depth of the soil column as shown in Figure 1, while keeping them constant in time. The carbon content in a soil profile typically decreases with soil depth (Ebrahimi & Or, 2016; Poage & Feng, 2004) since the majority of carbon input is delivered as plant litter in the topsoil and thereafter redistributed due to bioturbation and preferential transport in macropores. Similarly to Ebrahimi and Or (2016), we thus assume a steady-state, normalized carbon profile, which summarizes all such processes and exponentially decays with the soil depth, that is, $\bar{c}_{POM}(z) = e^{-6z},\ z \in [0, 0.5]$ m. This exponential type is in accordance with experimental studies as shown, for example, in Angers and Recous (1997), Bernoux et al. (1998), or Poage and Feng (2004). This POM input profile is used for the initial addition of POM to the system when creating the initial dispersed state (Figure 2a) and as continuous POM input over time in the microscale model (Figure 2c) as described in Section 2.4.3.

For the water saturation S, we consider, also similar to the wet situation in Ebrahimi and Or (2016), a steady-state exponential profile by $S(z) = 1 - e^{-14z},\ z \in [0, 0.5]$ m such that the saturation at the top of the profile is 0 and increases exponentially with soil depth. Since a higher water saturation correlates with a lower oxygen concentration, we set the normalized oxygen concentration as $\bar{c}_{O_2}(z) = e^{-14z},\ z \in [0, 0.5]$ m. From the continuous macroscopic environmental conditions, we use the value at the top of each discrete layer i, that is, at $z = (i - 1) \times 0.05$ m, to parameterize micro- and macroscale models.

The extension to more realistic, temporally changing conditions is straightforward, but beyond the scope of this research, as we focus here on the coupling of microscale information to macroscale diffusive transport of CO_2. The prescribed, spatially heterogeneous conditions already allow us to study the effects of such variations in principle.

2.4.2 | Macroscale model

In the macroscale model, we describe the diffusion of CO_2 through the soil column with Equations (1) and (2), introduced in Section 2.2, including the source term f^{micro}, which takes into account the amount of CO_2 produced at the microscale. We estimate the effective diffusion tensor D_i in layer i via the semi-empirical model by Millington and Quirk (1961):

$$D_i = D_g(\theta_i) = \frac{(\phi - \theta_i)^{\frac{10}{3}}}{\phi^2} D_g^0, \tag{4}$$

with the volumetric water content θ_i in layer i, the total porosity ϕ, and the molecular diffusion of CO_2 in the air $D_g^0 = 0.16\ cm^2\ s^{-1}$ (Rumble, 2022). Depending on the saturation level in the macroscopic profile and the given constant porosity ϕ of 0.35, we calculate a specific layer-dependent effective gas diffusion coefficient, which remains constant with respect to time. For a soil depth $z > 0.2$ m, where water saturation $S > 0.94$, this would result in values 10^4 smaller than the effective gas diffusion coefficient in air and thus smaller than the effective diffusion coefficient in water. For this reason, we set the effective gas diffusion

coefficient to the effective diffusion coefficient of CO_2 in water in all deeper layers, namely, 3.95E−6 $cm^2\ s^{-1}$.

2.4.3 | Microscale model and environmental conditions

As outlined above, we consider three types of POM addition to the microscale domain Y_{Ω_i}: the initial POM input, a continuous POM input over time due to the spatially decreasing carbon content along the soil profile, and—depending on the scenario—eventually an additional POM input retrieved from the overlying layer. First, we prescribe the layer-dependent initial POM addition to the microscale domain Y_{Ω_i}. We consider a maximum initial amount of POM of 3.60 mg C g^{-1} as in Zech, Schweizer, et al. (2022) based on 3D information from natural soils. This value corresponds to an addition of POM particles amounting to 2% of the solid. Assuming a POM density of 1.2 g cm^{-3} (according to Christensen, 1992) and solid density of 2.65 g cm^{-3}, the density of quartz corresponded to a POM content of 9.01 mg C g^{-1} and, assuming an OC mass fraction of 40% in POM, a resulting initial amount of 3.60 mg C g^{-1} as POM-OC. For comparison, OC input of 13 mg C g^{-1} in the form of POM in sizes <63 and 63 µm to 2 mm was added in incubation experiments by Bucka et al. (2021). Others added 5–30 mg C g^{-1} (De Gryze et al., 2005) or 5 mg C g^{-1} (Angers & Recous, 1997).

By multiplication with the exponentially decaying carbon profile $\bar{c}_{POM}$ described above, the initial POM addition over the soil profile was then given by $3.60 \times e^{-6z}$ mg C g^{-1}, $z \in [0, 0.5\ \text{m}]$. Second, for the continuous POM input over time, we consider the "high input" setting of Zech, Schweizer, et al. (2022) corresponding to annual OC input rates of 11.9 mg C g^{-1} as the basis. Over the soil depth z, the input rate is then calculated by $11.0 \times e^{-6z}$ mg C g^{-1} / year, $z \in [0, 0.5\ \text{m}]$, and the respective amount of POM input is continuously added in each layer over time.

For the half-saturation constant of oxygen, we consider $K_{O_2} = 10^{-3}$ mg L^{-1} (Ebrahimi & Or, 2016) and a maximum oxygen concentration of 0.1 mg L^{-1} corresponding to the maximum O_2 concentration at the aggregate boundary in Ebrahimi and Or (2016). Taking into account the environmental condition $\bar{c}_{O_2}$, we therefrom calculate the decreasing depth-dependent oxygen concentration by $0.1 \times e^{-14z}$ mg l^{-1}, $z \in [0, 0.5\ \text{m}]$. All other parameters related to the decomposition of POM were chosen as described in Zech, Schweizer, et al. (2022).

2.4.4 | Scenarios

We now illustrate the capability of our modeling approach by conducting a proof-of-concept study. We put the emphasis on the effects of transferring microscale information to the diffusive macroscale transport model, on the impact of texture on carbon turnover, and on the effect of spatially variable environmental conditions. We consider three different soil columns, which vary in the prescribed soil texture. Similar to the investigations in Zech, Schweizer, et al. (2022), we first take into account particle size distributions based on a clay content of 18% and 33% and assume a constant clay content over the depth in two columns. In each layer i of these two soil columns, we use the same initial distribution for the representative underlying microscale domain. The third profile is a mixture of the profiles, with the top half having a clay content of 18% and the bottom half having a clay content of 33%.

Furthermore, we evaluate three different options for the transport of unbound POM particles to lower layers, which can be interpreted as particulate leaching. In the reference setting, we only take into account the initial POM concentrations and the continuous input due to environmental conditions as outlined in Section 2.4.3. No additional transfer of mobile POM to deeper layers takes place. In addition, we consider two variants including a transport of all POM particles to the subsequent layer that were unbound for either 1 or 2 consecutive days. This choice corresponds to the two smallest possible time steps according to our temporal discretization with step size 1 day. The choice of larger time intervals revealed that almost no POM was unbound for such time spans, that is, such situations are already covered by the reference setting. In the deepest layer, no POM exits the system, except by degradation.

In total, this results in nine different scenarios simulated over 1000 days with a time step of one day. We perform 10 repetitions each to minimize randomness in the initial choice of the shapes and the placement of particles, as well as in the steps of the CAM. The ordinary differential equations were solved exactly, while standard finite element methods were used to solve the macroscopic diffusion equation.

3 | RESULTS

The results of the microscale model simulations (Figure 1b) are presented in Figure 4. The net input of POM in each layer, that is, the sum of initial POM input, continuous input over time and potential input from the upper layer minus the transferred POM to the lower layer, is visualized in Figure 4a. Transport of free POM particles to lower layers after 1 day leads to a decrease of the net POM input in the top layer of 29.6% (18% clay; dashed red line, Figure 4a) and 12.9% (33% clay; dashed blue line, Figure 4a), compared to the reference setting without transfer (continuous lines in Figure 4a). Note that in the reference setting the POM inputs coincide for the three textures, thus the continuous lines in Figure 4a overlap. Removal after 2 days leads to a smaller decrease of net POM input in the top layer (13.6% for 18% clay; red dotted line in Figure 4a; 3.1% for 33% clay; blue dotted line in Figure 4a). For all lower layers, that is, for $z > 0.05$ m, the transfer of POM from upper layers leads to a minor increase in net POM input. Generally, for the texture with 18% clay (red lines), the transport of free POM particles to deeper layers is enhanced. For the mixed soil profile (green lines in Figure 4), the net POM input in the upper half layers coincides with the one of the low clay profile by design. In the first layer with higher clay content in the mixed profile ($z \in [0.25\ \text{m}, 0.3\ \text{m}]$), the net POM input is significantly increased, compared to both uniform profiles for removal after 1 day (23.0% higher, compared to 18% clay, 33.1% for 33% clay). In the

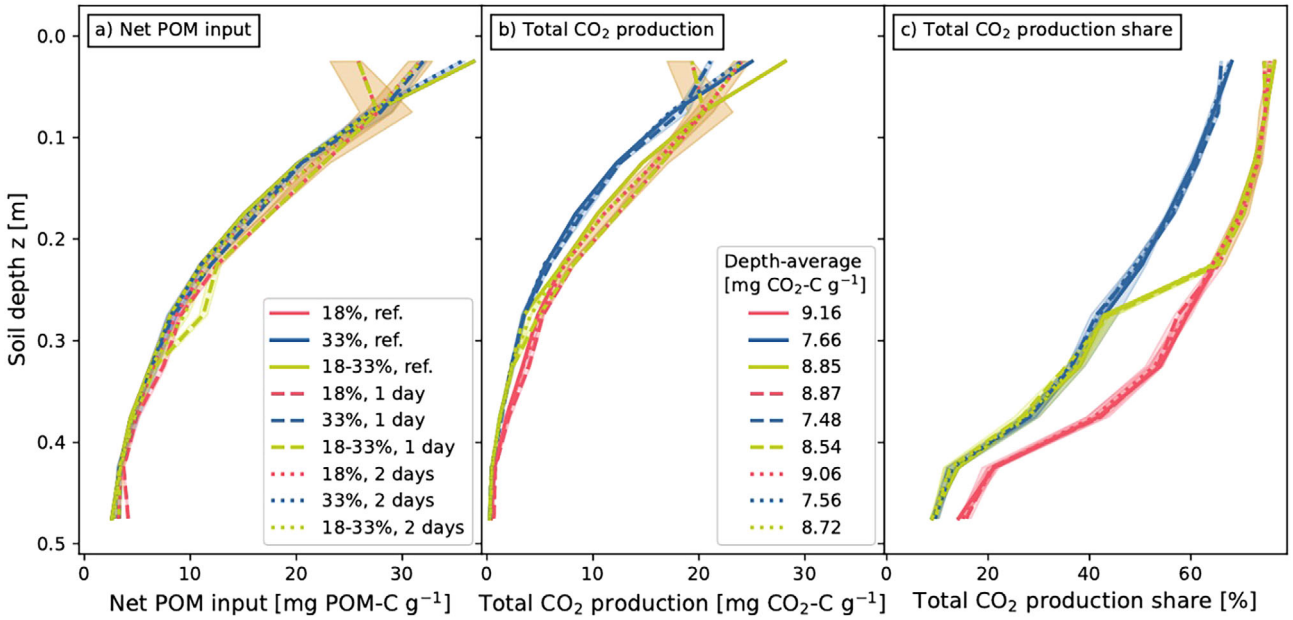

FIGURE 4 Net POM input (a), total produced CO_2 (b), and share of net POM input that was respired as CO_2 (c) over soil depth z as a result of the microscale model in different scenarios. Median of 10 repetitions with error band representing lower and upper quartile.

lower layers ($z > 0.3$ m), the net POM input approaches the 33% clay profile.

In Figure 4b, the total amount of respired CO_2 after 1000 days of the microscale model for each layer is visualized. Lower clay content (red lines) in general results in higher CO_2 production, for example, averaged over the total profile 9.16 mg CO_2-C g^{-1} are produced in the reference setting for 18% clay (red continuous line in Figure 4b) and 7.66 mg CO_2-C g^{-1} for 33% clay (blue continuous line). The differences in CO_2 production between the distinct removal settings qualitatively mirror the net POM input profile in Figure 4a, that is, the scenarios with removal lead to lower CO_2 production in the uppermost layers and higher CO_2 production in the lower layers. In total, however, faster transfer of POM to lower layers results in a decrease in CO_2 production (averaged over profile for 18% clay: 8.87 mg CO_2-C g^{-1} for removal after 1 day, red dashed line in Figure 4b, compared to 9.16 mg CO_2-C g^{-1} without removal, red continuous line). As for the net POM input, the amount of carbon produced in the mixed soil profile coincides with the top half of the low clay profile by design. Toward the bottom, the amount of produced carbon in the mixed profile approaches the one of the high clay profile and generally lies in between the two uniform profiles. Even in the first layer in which the clay content changes (Layer 6) and the net POM input in the mixed profile is increased, compared to the low clay profile (by 23.0%), the amount of produced CO_2 is reduced (by 6.6%). In Figure 4c, the share of net carbon input respired as CO_2 is visualized over the profile depth. For the 18% clay profile, the share of carbon respired as CO_2 decreases from 76.6% in the top layer to 14.1% in the bottom layer, and for the 33% clay profile, it decreases from 68.1% to 8.9%. The differences between the two textures reflect the differences in absolute total CO_2 production outlined above.

Due to the initial and boundary conditions and the design of the scenarios, the microscale simulations induce an outflow of CO_2 at the top of the macroscopic domain. The remaining CO_2 contents in the soil profiles after 200, 600, and 1000 days of the macroscale model (Figure 1c) are visualized in Figure 5. The macroscopic distribution of CO_2 (Figure 5) significantly differs from the input profile according to the microscale simulation (Figure 4b). In the input profile, the amount of totally produced CO_2 monotonously decreases with soil depth (Figure 4b). In comparison, in the macroscale profile, the CO_2 content peaks at approximately $z = 0.3$ m and decreases monotonously toward the bottom and top of the profile. In the topmost layers, that is, for a soil depth $z < 0.15$ m, almost no volatile CO_2 was present in all scenarios at $t = 1000$ days.

For all layers, the macroscopic profile with a clay content of 18% (red lines in Figure 5) shows a higher content of CO_2 mirroring the CO_2 input profile from the microscale simulations (Figure 4b). Fast daily transfer of POM in the microscale simulations (red dashed lines in Figure 5) leads to the highest CO_2 content in the lower layers of the macroscale profile for the clay content of 18% and thus higher total CO_2 content (Figure 5). At the clay content of 33% (blue lines in Figure 5), there are no significant differences between the three different removal settings. In the mixed setting, the CO_2 content lies generally between the two uniform columns similar to the CO_2 produced in the microscale simulations. As with the 18% clay profile, the faster transfer of free POM particles results in an increase in CO_2 content (dashed vs. dotted and continuous yellow lines in Figure 5).

In Figure 6, the relative amount of POM that is attached to reactive or memory edges is depicted. Overall, our forward simulations result in 60%–85% of POM surfaces (edges) in contact with gluing soil particles. Note that edge contacts are counted individually, that is, a POM particle where 50% of its edges are attached to reactive or memory edges will not count as 100% attached but 50%. It is evident that the variance decreases with simulation time, that is, some stationary

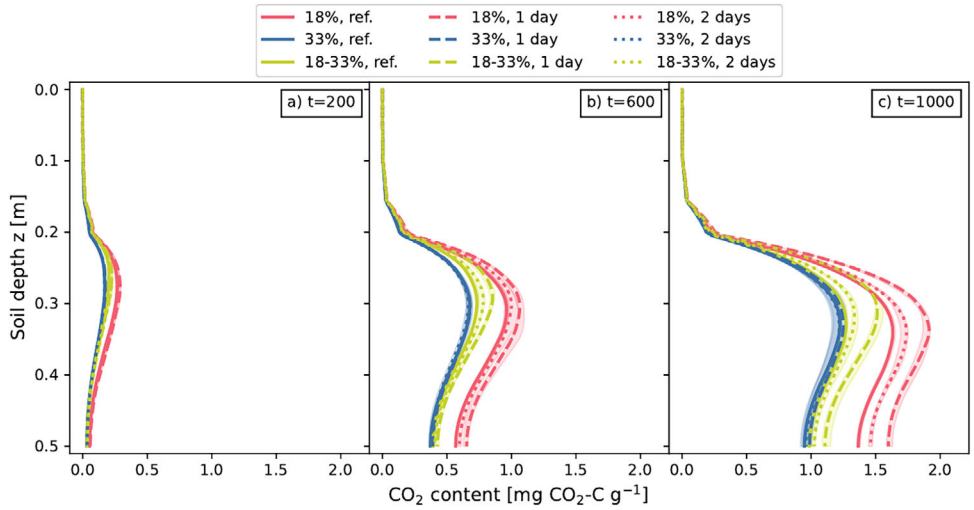

FIGURE 5 Macroscopic profile of remaining CO_2 content after 200 (a), 600 (b), and 1000 (c) days. Median of 10 repetitions with error band representing lower and upper quartile.

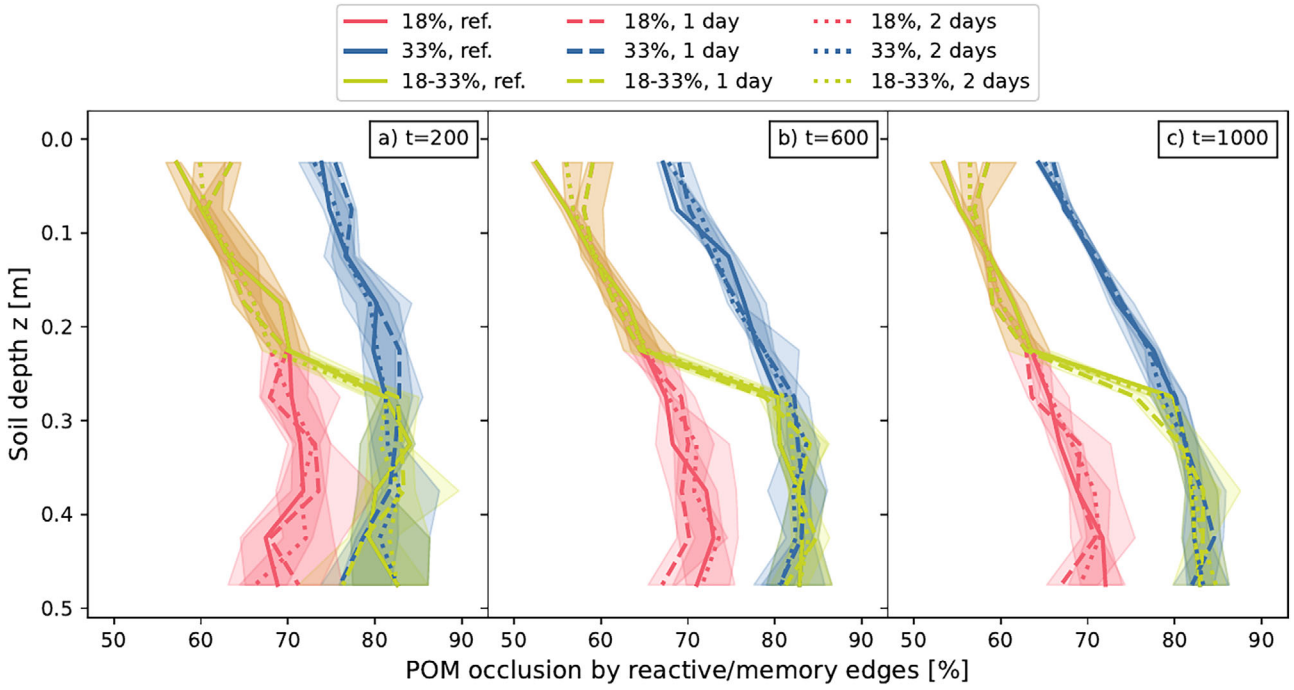

FIGURE 6 Percentage of POM edges attached to reactive or memory edges of soil particles over depth profile after 200 (a), 600 (b), and 1000 (c) days. Median of 10 repetitions with error band representing lower and upper quartile.

state is reached for larger times. The reference (solid lines in Figure 6), 1-day (dashed lines) and 2-day scenarios (dotted lines) do not differ significantly. However, the share of attached surfaces is larger for higher clay content (blue lines) as well as for deeper layers.

Finally, we calculate that part of the produced CO_2 in the whole soil profile, which remained in the soil at the end of the simulations after 1000 days. Among the nine scenarios, this part sums up to 7.24%–10.78% of the produced CO_2. The highest value occurs for the 18% clay texture and the daily POM transfer.

4 | DISCUSSION

The microscale simulations show in all settings that a higher clay content leads to lower CO_2 respiration. In the case of the reference setting without transfer, this is consistent with the texture effects observed experimentally in Bucka et al. (2021), Witzgall et al. (2021), and Schweizer et al. (2021). A higher clay content provides a greater number of reactive surfaces and thus delays the turnover of POM into CO_2 by structural occlusion. This correlation of higher clay content

and higher OC concentrations due to more mineral-associated OC has been reported in many studies, see, for example, the meta-analysis in Laganière et al. (2010). This is emphasized by the lower share of produced CO_2 in all layers (Figure 4c).

The transfer of free POM particles to deeper layers resulted in a decrease in net POM input mainly in the top layer for all soil columns. In all other layers, the differences are small irrespective of the depth and absolute amount of POM in the layer. This indicates that the majority of the POM particles came into contact with reactive or memory edges very quickly and that structural stabilization/occlusion of POM occurred rapidly. This is in line with observations from large data synthesis studies with more than 1144 globally distributed soil profiles (Sokol et al., 2022), where around 80% of total soil organic carbon was considered as mineral-associated in topsoil (0–30 cm) and subsoil (30–120 cm) of croplands, with highest values in temperate climates. The value of 60%–85% of POM edges attached to reactive or memory edges of soil particles (see Figure 6) yields realistic results from the forward simulation. Comparing the two textures, the transfer of free POM to deeper layers resulted in a decrease of net POM input in the top layer for the low clay profile and a slight increase in the deeper layers, compared to the high clay profile. This can be explained by the higher amount of small clay particles and correspondingly higher total surface area and thus better potential to structurally stabilize POM (Schweizer et al., 2021) and prevent its transfer to deeper layers.

Overall, the higher clay content resulted in lower CO_2 production in the removal settings. This indicates that the texture effect with respect to POM decomposition outweighed the texture effect with respect to the removal of free POM to deeper layers. Although POM transfer had an effect on CO_2 production as described above, it was relatively small. Consequently, other mechanisms for POM transfer to deeper layers have a larger impact, such as transport through macropores, bioturbation due to earthworm activities, and so forth (Guhra et al., 2022).

Nonetheless, in the lower half of the soil profiles, the accumulation of CO_2 is the largest, even though production is low due to limited oxygen and POM supply. This demonstrates that transport processes toward the surface are not fast enough to balance the production rate there and the overall regime is diffusion-limited there.

Bucka et al. (2021) report an accumulated CO_2-C release during the incubation period of their experiments (with the Cambiosol soils), which increased with higher sand contents with a mean value of 1.6 $\pm$ 0.4 mg g^{-1} in the clay loam, 1.9 $\pm$ 0.1 mg g^{-1} in the loam, and 2.1 $\pm$ 0.2 mg g^{-1} in the sandy loam. Although the experiment design and duration were different (95 days, 30 days of incubation), and also no measurements in the profile are available, the results are consistent with our simulated data: During 1000 days, a CO_2-C production in the range of 1–20 mg CO_2-C g^{-1} was observed (Figure 4b). Also, production and accumulation are highest for the coarse textured soil (red lines in Figures 4 and 5).

In general, the CO_2 production in the microscale model, which was used as a source term for the macroscale model, decreased with soil depth. On the one hand, POM content was lower as outlined above, and on the other hand, this is due to the decreasing oxygen content leading to a decrease in POM decomposition with depth.

In summary, the CO_2 production is determined by:

- texture effects due to fast structural occlusion of POM and limited POM transfer and
- macroscopic environmental conditions such as limited oxygen availability.

Due to the increasing saturation with soil depth, the effective gas diffusion coefficient also decreased with depth. These two factors led to a rapid release of CO_2 in the upper layers of the profile, where almost no CO_2 accumulated. In larger depths, the results are multifaceted. At depths $z > 0.2$ m, where water saturation $S > 0.94$ and diffusion became a limiting factor, CO_2 began to accumulate in the profile (recall Figure 5) despite the lower amounts of POM and O_2 and smaller production there (cf. Figure 4). While the faster transfer of POM to deeper layers in the microscale simulations led even to a small decrease in total CO_2 production as described above, in the macroscale profile, the total remaining CO_2 content after 1000 days nevertheless increased for the faster transfer settings. This was mainly due to a higher accumulation of CO_2 in the deeper layers of the macroscale profile where diffusion was limited. The effect was most pronounced if free POM was propagated daily to the deeper layers and for the 18% clay (Figure 5, red curves) although the net POM input was very similar (Figure 4a). The coupling of the pore-scale carbon turnover to the profile scale CO_2 diffusion reveals that 7%–10% (most significant for low clay content and fast transfer setting) of the produced CO_2 remains in the soil. This shows that due to the interplay of counteracting factors at the macroscale, a simple summation of produced CO_2 over depth does not represent the macroscopic profiles. Thus, the subsequent macroscale transport model provides additional valuable insights into the time-dependent CO_2 release from soil profiles, in particular, if amended with realistic soil profile scenarios.

5 | CONCLUSION

In summary, the coupled simulation of macroscopic transport and pore-scale carbon and aggregate turnover reveals the complex, nonlinear interplay of the underlying processes. Limitations by diffusive transport, oxygen availability, texture-dependent occlusion, and turnover of OM drive CO_2 production and carbon storage. Our results underline the capability of our model to investigate the opposing factors, which determine the nonlinear distribution of CO_2 in the soil profile. This emphasizes the need for micro–macro models exchanging information on different scales to investigate and quantify the effects of structural changes, variations in environmental conditions, or differences in the degradation processes in the hot spots of soils on carbon turnover (Baveye et al., 2018; Gerke et al., 2022; Pot et al., 2022b; Vereecken et al., 2016). This explicit spatially and temporally dynamic model contributes to understanding the linkage between soil architecture and functions from the micron to the pedon scale.

We emphasize that the simulation studies do not comprise any fitting parameters but that all results are obtained from forward simulations with realistic, process-based assumptions and parameter sets derived from experimental findings.

In this proof-of-concept study, some conditions were simplified to reduce the overall complexity and to facilitate the interpretation of the observed system. However, the general modular concept can be easily adapted and extended for further influencing factors. The systematic study of any type of macroscopic environmental conditions, more realistic and changeable soil textures, different microbial communities, or different types of OM is straightforward. As outlined, for instance, in Ebrahimi and Or (2016), limited nutrient diffusion to microbes due to low saturation at the top of the soil profile can likewise lead to nonlinear profiles in microscale CO_2 production.

Finally, model extensions to account for further POM transfer mechanisms into the subsoil such as through macropores are needed. Likewise, a more detailed macroscopic model for the transport of CO_2 is desirable taking into account also macropores and further inhomogeneities at the macro scale. Another extension of the presented model is the generalization to a two-way coupling of scales. This may also include oxygen dynamics depending on transport across the macroscale profile and its consumption by microscale processes. Along this line, extensions to more realistic representations of microbial components are possible. Finally, extensions to a temporally changing saturation and seasonal cycles of POM input or more sophisticated heterogeneities in the soil profiles may certainly be the topic of future research.

ACKNOWLEDGMENTS

We gratefully acknowledge the financial support of the *Deutsche Forschungsgemeinschaft (DFG)* within the framework of the *research unit 2179 "MAD Soil—Microaggregates: Formation and turnover of the structural building blocks of soils," project* 276972051. We thank the reviewers for their helpful comments to improve the manuscript.

Open access funding enabled and organized by Projekt DEAL.

DATA AVAILABILITY STATEMENT

The data that support the findings of this study are available from the corresponding author upon reasonable request.

ORCID

Simon Zech https://orcid.org/0000-0002-0475-2651
Alexander Prechtel https://orcid.org/0000-0002-6982-2403
Nadja Ray https://orcid.org/0000-0002-9596-953X

REFERENCES

Angers, D. A., & Recous, S. (1997). Decomposition of wheat straw and rye residues as affected by particle size. *Plant and Soil*, *189*, 197–203.

Baveye, P. C., Otten, W., Kravchenko, A., Balseiro-Romero, M., Beckers, E., Chalhoub, M., Darnault, C., Eickhorst, T., Garnier, P., Hapca, S., Kiranyaz, S., Monga, O., Mueller, C. W., Nunan, N., Pot, V., Schlüter, S., Schmidt, H., & Vogel, H. J. (2018). Emergent properties of microbial activity in heterogeneous soil microenvironments: Different research approaches are slowly converging, yet major challenges remain. *Frontiers in Microbiology*, *9*, 1929. https://doi.org/10.3389/fmicb.2018.01929

Bernoux, M., Cerri, C. C., Neill, C., & de Moraes, J. F. (1998). The use of stable carbon isotopes for estimating soil organic matter turnover rates. *Geoderma*, *82*(1-3), 43–58.

Borden, R. C., & Bedient, P. B. (1986). Transport of dissolved hydrocarbons influenced by oxygen-limited biodegradation: 1. Theoretical development. *Water Resources Research*, *22*(13), 1973–1982.

Borkovec, M., Wu, Q., Sticher, H., Degovics, G., & Laggner, P. (1993). Surface area and size distributions of soil particles. In T. F. Tadros & J. Gregory (Eds.), *Colloids in the aquatic environment* (pp. 65–76). Elsevier.

Bucka, F. B., Kölbl, A., Uteau, D., Peth, S., & Kögel-Knabner, I. (2019). Organic matter input determines structure development and aggregate formation in artificial soils. *Geoderma*, *354*, 113881. https://doi.org/10.1016/j.geoderma.2019.113881

Bucka, F. B., Felde, V. J., Peth, S., & Kögel-Knabner, I. (2021). Disentangling the effects of OM quality and soil texture on microbially mediated structure formation in artificial model soils. *Geoderma*, *403*, 115213. https://doi.org/10.1016/j.geoderma.2021.115213

Chakrawal, A., Herrmann, A. M., Koestel, J., Jarsjö, J., Nunan, N., Kätterer, T., & Manzoni, S. (2020). Dynamic upscaling of decomposition kinetics for carbon cycling models. *Geoscientific Model Development*, *13*(3), 1399–1429.

Christensen, B. T. (1992). Physical fractionation of soil and organic matter in primary particle size and density separates. In B. A. Stewart (Ed.), *Advances in soil sciences* (Vol. 20, pp. 1–90). Springer.

Christensen, B. T. (2001). Physical fractionation of soil and structural and functional complexity in organic matter turnover. *European Journal of Soil Science*, *52*(3), 345–353.

Crawford, J. W., Deacon, L., Grinev, D., Harris, J. A., Ritz, K., Singh, B. K., & Young, I. (2012). Microbial diversity affects self-organization of the soil–microbe system with consequences for function. *Journal of the Royal Society Interface*, *9*(71), 1302–1310.

Crawford, J. W., Verrall, S., & Young, I. M. (1997). The origin and loss of fractal scaling in simulated soil aggregates. *European Journal of Soil Science*, *48*(4), 643–650.

De Gryze, S., Six, J., Brits, C., & Merckx, R. (2005). A quantification of short-term macroaggregate dynamics: Influences of wheat residue input and texture. *Soil Biology and Biochemistry*, *37*(1), 55–66.

Ebrahimi, A., & Or, D. (2016). Microbial community dynamics in soil aggregates shape biogeochemical gas fluxes from soil profiles–upscaling an aggregate biophysical model. *Global Change Biology*, *22*(9), 3141–3156.

Ebrahimi, A., & Or, D. (2018). On upscaling of soil microbial processes and biogeochemical fluxes from aggregates to landscapes. *Journal of Geophysical Research: Biogeosciences*, *123*(5), 1526–1547.

Felde, V. J., Schweizer, S. A., Biesgen, D., Ulbrich, A., Uteau, D., Knief, C., Graf-Rosenfellner, M., Kögel-Knabner, I., & Peth, S. (2021). Wet sieving versus dry crushing: Soil microaggregates reveal different physical structure, bacterial diversity and organic matter composition in a clay gradient. *European Journal of Soil Science*, *72*(2), 810–828.

Fernández-Ugalde, O., Barré, P., Hubert, F., Virto, I., Girardin, C., Ferrage, E., Caner, L., & Chenu, C. (2013). Clay mineralogy differs qualitatively in aggregate-size classes: Clay-mineral-based evidence for aggregate hierarchy in temperate soils. *European Journal of Soil Science*, *64*(4), 410–422.

Fernández-Ugalde, O., Barré, P., Virto, I., Hubert, F., Billiou, D., & Chenu, C. (2016). Does phyllosilicate mineralogy explain organic matter stabilization in different particle-size fractions in a 19-year C_3/C_4 chronosequence in a temperate Cambisol? *Geoderma*, *264*, 171–178.

Gerke, H. H., Vogel, H. J., Weber, T. K., Van der Meij, W. M., & Scholten, T. (2022). 3–4D soil model as challenge for future soil research: Quantitative soil modeling based on the solid phase. *Journal of Plant Nutrition and Soil Science*, *185*(6), 720–744.

Guhra, T., Stolze, K., & Totsche, K. U. (2022). Pathways of biogenically excreted organic matter into soil aggregates. *Soil Biology and Biochemistry*, *164*, 108483. https://doi.org/10.1016/j.soilbio.2021.108483

Keiluweit, M., Nico, P. S., Kleber, M., & Fendorf, S. (2016). Are oxygen limitations under recognized regulators of organic carbon turnover in upland soils? *Biogeochemistry*, *127*, 157–171.

Kuzyakov, Y., & Blagodatskaya, E. (2015). Microbial hotspots and hot moments in soil: Concept & review. *Soil Biology and Biochemistry*, *83*, 184–199.

Laganiere, J., Angers, D. A., & Pare, D. (2010). Carbon accumulation in agricultural soils after afforestation: A meta-analysis. *Global Change Biology*, *16*(1), 439–453.

Manzoni, S., Taylor, P., Richter, A., Porporato, A., & Ågren, G. I. (2012). Environmental and stoichiometric controls on microbial carbon-use efficiency in soils. *New Phytologist*, *196*(1), 79–91.

Mbé, B., Monga, O., Pot, V., Otten, W., Hecht, F., Raynaud, X., Nunan, N., Chenu, C., Baveye, P. C., & Garnier, P. (2022). Scenario modelling of carbon mineralization in 3D soil architecture at the microscale: Toward an accessibility coefficient of organic matter for bacteria. *European Journal of Soil Science*, *73*(1), e13144. https://doi.org/10.1111/ejss.13144

McCarthy, J. F., Ilavsky, J., Jastrow, J. D., Mayer, L. M., Perfect, E., & Zhuang, J. (2008). Protection of organic carbon in soil microaggregates via restructuring of aggregate porosity and filling of pores with accumulating organic matter. *Geochimica et Cosmochimica Acta*, *72*(19), 4725–4744.

Meurer, K., Barron, J., Chenu, C., Coucheney, E., Fielding, M., Hallett, P., Herrmann, A. M., Keller, T., Koestel, J., Larsbo, M., Lewan, E., Or, D., Parsons, D., Parvin, N., Taylor, A., Vereecken, H., & Jarvis, N. (2020). A framework for modelling soil structure dynamics induced by biological activity. *Global Change Biology*, *26*(10), 5382–5403.

Millington, R. J., & Quirk, J. P. (1961). Transport in porous media. In F. A. van Baren (Ed.), *Transactions of 7th International Congress of Soil Science International Society of Soil Science* (Vol. I, pp. 97–106).

Nunan, N. (2017). The microbial habitat in soil: Scale, heterogeneity and functional consequences. *Journal of Plant Nutrition and Soil Science*, *180*(4), 425–429.

Poage, M. A., & Feng, X. (2004). A theoretical analysis of steady state $\delta^{13}C$ profiles of soil organic matter. *Global Biogeochemical Cycles*, *18*(2). https://doi.org/10.1029/2003GB002195

Portell, X., Pot, V., Garnier, P., Otten, W., & Baveye, P. C. (2018). Microscale heterogeneity of the spatial distribution of organic matter can promote bacterial biodiversity in soils: Insights from computer simulations. *Frontiers in Microbiology*, *9*, 1583. https://doi.org/10.3389/fmicb.2018.01583

Pot, V., Portell, X., Otten, W., Garnier, P., Monga, O., & Baveye, P. C. (2022a). Understanding the joint impacts of soil architecture and microbial dynamics on soil functions: Insights derived from microscale models. *European Journal of Soil Science*, *73*(3), e13256. https://doi.org/10.1111/ejss.13256

Pot, V., Portell, X., Otten, W., Garnier, P., Monga, O., & Baveye, P. C. (2022b). Accounting for soil architecture and microbial dynamics in microscale models: Current practices in soil science and the path ahead. *European Journal of Soil Science*, *73*(1), e13142.

Ray, N., Rupp, A., & Prechtel, A. (2017). Discrete-continuum multiscale model for transport, biomass development and solid restructuring in porous media. *Advances in Water Resources*, *107*, 393–404.

Ray, N., Rupp, A., Schulz, R., & Knabner, P. (2018). Old and new approaches predicting the diffusion in porous media. *Transport in Porous Media*, *124*, 803–824.

Roose, T., Keyes, S. D., Daly, K. R., Carminati, A., Otten, W., Vetterlein, D., & Peth, S. (2016). Challenges in imaging and predictive modeling of rhizosphere processes. *Plant and Soil*, *407*, 9–38.

Rumble, J. R. (2022). *CRC handbook of chemistry and physics* (103rd ed.). CRC Press/Taylor & Francis.

Rupp, A., Guhra, T., Meier, A., Prechtel, A., Ritschel, T., Ray, N., & Totsche, K. U. (2019). Application of a cellular automaton method to model the structure formation in soils under saturated conditions: A mechanistic approach. *Frontiers in Environmental Science*, *7*, 170. https://doi.org/10.3389/fenvs.2019.00170

Schjønning, P., Thomsen, I. K., Møberg, J. P., de Jonge, H., Kristensen, K., & Christensen, B. T. (1999). Turnover of organic matter in differently textured soils: I. Physical characteristics of structurally disturbed and intact soils. *Geoderma*, *89*(3-4), 177–198.

Schmidt, M. W., Torn, M. S., Abiven, S., Dittmar, T., Guggenberger, G., Janssens, I. A., Kleber, M., Kögel-Knabner, I., Lehmann, J., Manning, D. A. C., Nanniperi, P., Rasse, D. P., Weiner, S., & Trumbore, S. E. (2011). Persistence of soil organic matter as an ecosystem property. *Nature*, *478*(7367), 49–56.

Schweizer, S. A., Bucka, F. B., Graf-Rosenfellner, M., & Kögel-Knabner, I. (2019). Soil microaggregate size composition and organic matter distribution as affected by clay content. *Geoderma*, *355*, 113901. https://doi.org/10.1016/j.geoderma.2019.113901

Schweizer, S. A., Mueller, C. W., Höschen, C., Ivanov, P., & Kögel-Knabner, I. (2021). The role of clay content and mineral surface area for soil organic carbon storage in an arable toposequence. *Biogeochemistry*, *156*(3), 401–420.

Sokol, N. W., Whalen, E. D., Jilling, A., Kallenbach, C., Pett-Ridge, J., & Georgiou, K. (2022). Global distribution, formation and fate of mineral-associated soil organic matter under a changing climate: A trait-based perspective. *Functional Ecology*, *36*(6), 1411–1429.

Stockmann, U., Adams, M. A., Crawford, J. W., Field, D. J., Henakaarchchi, N., Jenkins, M., Minasny, B., McBratney, A. B., de Remy de Courcelles, V., Singh, K., Wheeler, I., Abbott, L., Angers, D. A., Baldock, J., Bird, M., Brookes, P. C., Chenu, C., Jastrow, J. D., Lal, R., … Zimmermann, M. (2013). The knowns, known unknowns and unknowns of sequestration of soil organic carbon. *Agriculture, Ecosystems & Environment*, *164*, 80–99.

Tang, Y., & Valocchi, A. J. (2013). An improved cellular automaton method to model multispecies biofilms. *Water Research*, *47*(15), 5729–5742.

Totsche, K. U., Amelung, W., Gerzabek, M. H., Guggenberger, G., Klumpp, E., Knief, C., Lehndorff, E., Mikutta, R., Peth, S., Prechtel, A., Ray, N., & Kögel-Knabner, I. (2018). Microaggregates in soils. *Journal of Plant Nutrition and Soil Science*, *181*(1), 104–136.

Vereecken, H., Schnepf, A., Hopmans, J. W., Javaux, M., Or, D., Roose, T., Vanderborght, J., Young, M. H., Amelung, W., Aitkenhead, M., Allison, S. D., Assouline, S., Baveye, P., Berli, M., Brüggemann, N., Finke, P., Flury, M., Gaiser, T., Govers, G., … Young, I. M. (2016). Modeling soil processes: Review, key challenges, and new perspectives. *Vadose Zone Journal*, *15*(5), vzj2015.09.0131. https://doi.org/10.2136/vzj2015.09.0131

Witzgall, K., Vidal, A., Schubert, D. I., Höschen, C., Schweizer, S. A., Buegger, F., Pouteau, V., Chenu, C., & Mueller, C. W. (2021). Particulate organic matter as a functional soil component for persistent soil organic carbon. *Nature Communications*, *12*(1), 4115. https://doi.org/10.1038/s41467-021-24192-8

Zech, S., Dultz, S., Guggenberger, G., Prechtel, A., & Ray, N. (2020). Microaggregation of goethite and illite evaluated by mechanistic modeling. *Applied Clay Science*, *198*, 105845. https://doi.org/10.1016/j.clay.2020.105845

Zech, S., Ritschel, T., Ray, N., Totsche, K. U., & Prechtel, A. (2022). How water connectivity and substrate supply shape the turnover of organic matter—Insights from simulations at the scale of microaggregates. *Geoderma*, *405*, 115394. https://doi.org/10.1016/j.geoderma.2021.115394

Zech, S., Schweizer, S. A., Bucka, F. B., Ray, N., Kögel-Knabner, I., & Prechtel, A. (2022). Explicit spatial modeling at the pore scale unravels the interplay of soil organic carbon storage and structure dynamics. *Global Change Biology*, *28*(15), 4589–4604.

How to cite this article: Zech, S., Prechtel, A., & Ray, N. (2024). Coupling scales in process-based soil organic carbon modeling including dynamic aggregation. *Journal of Plant Nutrition and Soil Science*, *187*, 130–142. https://doi.org/10.1002/jpln.202300080